Acta Crystallographica Section D
Biological Crystallography
ISSN 0907-4449

High-resolution crystal structure of the catalytic domain of human dual-specificity phosphatase 26

Eun-Young Won,[a,b]‡ Yong Xie,[c]‡§ Chie Takemoto,[c] Lirong Chen,[d] Zhi-Jie Liu,[d] Bi-Cheng Wang,[d] Daeyoup Lee,[a] Eui-Jeon Woo,[b] Sung Goo Park,[b] Mikako Shirouzu,[c] Shigeyuki Yokoyama,[c] Seung Jun Kim[b]* and Seung-Wook Chi[b]*

[a]Department of Biological Sciences, Korea Advanced Institute of Science and Technology, Daejeon 305-701, Republic of Korea, [b]Medical Proteomics Research Center, KRIBB, Daejeon 305-806, Republic of Korea, [c]RIKEN Systems and Structural Biology Center, Tsurumi, Yokohama 230-0045, Japan, and [d]Department of Biochemistry and Molecular Biology, University of Georgia, Athens, GA 30603, USA

‡ These authors contributed equally to this work.
§ Present address: Institute of Medicinal Plant Development, Chinese Academy of Medical Science and Peking Union Medical College, Malianwa North Road, Haidian District, Beijing 100193, People's Republic of China.

Correspondence e-mail: ksj@kribb.re.kr, swchi@kribb.re.kr

Received 11 September 2012
Accepted 19 February 2013

PDB References: DUSP26-C, 2e0t; C152S mutant, 4b04

Dual-specificity phosphatases (DUSPs) play an important role in regulating cellular signalling pathways governing cell growth, differentiation and apoptosis. Human DUSP26 inhibits the apoptosis of cancer cells by dephosphorylating substrates such as p38 and p53. High-resolution crystal structures of the DUSP26 catalytic domain (DUSP26-C) and its C152S mutant [DUSP26-C (C152S)] have been determined at 1.67 and 2.20 Å resolution, respectively. The structure of DUSP26-C showed a novel type of domain-swapped dimer formed by extensive crossover of the C-terminal α7 helix. Taken together with the results of a phosphatase-activity assay, structural comparison with other DUSPs revealed that DUSP26-C adopts a catalytically inactive conformation of the protein tyrosine phosphate-binding loop which significantly deviates from that of canonical DUSP structures. In particular, a noticeable difference exists between DUSP26-C and the active forms of other DUSPs at the hinge region of a swapped C-terminal domain. Additionally, two significant gaps were identified between the catalytic core and its surrounding loops in DUSP26-C, which can be exploited as additional binding sites for allosteric enzyme regulation. The high-resolution structure of DUSP26-C may thus provide structural insights into the rational design of DUSP26-targeted anticancer drugs.

1. Introduction

Protein tyrosine phosphorylation is a fundamental regulation mechanism for a wide variety of cellular signalling pathways and other physiological processes (Tonks, 2006). This post-translational modification process is reversibly regulated *via* reciprocal phosphorylation and dephosphorylation, which are mediated by protein tyrosine kinases (PTKs) and protein tyrosine phosphatases (PTPs), respectively (Hunter, 1995; Pawson, 1995). A total of 107 PTP superfamily members have been identified in the human genome. Class I cysteine-based PTPs are the most populated group, with 99 members that are classified into two distinct groups based on substrate specificity (Alonso *et al.*, 2004): classical tyrosine-specific PTPs, with 38 members, and dual-specificity phosphatases (DUSPs), with 61 members. DUSPs are a diverse family of PTPs that can dephosphorylate both phosphoserine/threonine and phosphotyrosine residues (Alonso *et al.*, 2004). DUSPs play an important role in regulating cellular signalling pathways governing cell growth, differentiation and apoptosis (Patterson *et al.*, 2009). DUSPs act on a wide range of substrates, including mRNA, inositol phospholipids, phosphoserine, phosphothreonine and phosphotyrosine. Typical DUSPs contain a catalytic domain and a mitogen-activated protein kinase

(MAPK)-binding (MKB) domain (Farooq & Zhou, 2004). In contrast, atypical DUSPs contain a catalytic domain similar to that of typical DUSPs but lack a substrate-binding domain (Alonso *et al.*, 2004). Although substrate specificities vary across the different DUSPs, they share a common catalytic mechanism mediated by a catalytic triad composed of a cysteine residue, an arginine residue and an aspartic acid residue, and a highly conserved consensus motif in the active site referred to as the HC*xx*G*xx*RS(T) motif. The substrate specificity of PTPs is mainly determined by the shape, size and depth of the catalytic pocket (Denu *et al.*, 1996). In contrast to classical tyrosine-specific PTPs, DUSPs have a relatively shallow and broad binding pocket that is only ∼6 Å deep in order to accommodate both phosphoserine/threonine and phosphotyrosine residues (Zhou *et al.*, 1994).

Many human diseases such as diabetes, metabolic syndrome and cancer are caused by defective PTP function, suggesting that human PTPs are important therapeutic targets for drug development. However, the development of clinically effective inhibitors of human PTPs is challenging because of the difficulties in achieving sufficient specificity and/or bioavailability (Zhang & Zhang, 2007; Blaskovich, 2009), which are attributable to the shallow catalytic pocket, the high similarity in the structures and the highly charged character of PTP active sites. Recently, Wiesmann and coworkers identified an allosteric site other than the catalytic site in the PTP1B structure that could be used to develop a therapeutic drug for diabetes (Wiesmann *et al.*, 2004). Thus, the strategy of targeting allosteric sites of PTPs may result in increased specificity and efficacy of inhibition. In this context, determination of the three-dimensional structures of PTPs plays an important role in providing structural insights into their functions and regulation mechanism, thus contributing to structure-based drug design (Almo *et al.*, 2007; Hoffman *et al.*, 2004; Kim *et al.*, 2007).

DUSP26 is also known as mitogen-activated protein kinase phosphatase-8 (MKP-8), low-molecular-mass DUSP-4 (LDP-4) and stress-activated protein kinase pathway-regulating phosphatase 3 (SKRP3). As a member of the atypical DUSP family, DUSP26 contains a conserved catalytic domain (residues 61–211) and an additional N-terminal region (residues 1–60). DUSP26 is located predominantly within the nucleus (Vasudevan *et al.*, 2005; Takagaki *et al.*, 2007), although it is also found in the cytosol of PC12 cells (Wang *et al.*, 2006). DUSP26 is mainly expressed in the brain (Hu & Mivechi, 2006; Takagaki *et al.*, 2007), particularly in neurons (Hu & Mivechi, 2006), with its expression also being enriched in the skeletal muscle, prostate and ovaries. DUSP26 may play an important role in tumorigenesis and in the progression of embryonal cancers. DUSP26 is located at 8p12, a chromosomal region that has been shown to be amplified in anaplastic thyroid cancer (ATC); thus, the phosphatase is overexpressed in ATC cells. DUSP26 promotes the survival of ATC cells by dephosphorylating p38 MAPK, thereby inhibiting p38-mediated apoptosis (Yu *et al.*, 2007). In addition, this phosphatase has been found in wild-type p53-containing cancer cell lines such as neuroblastoma, neuroepithelioma and retinoblastoma (Tanuma *et al.*, 2009). DUSP26 binds to and dephosphorylates p53 at Ser20 and Ser37 to inhibit the p53 tumour suppressor function and thus induces resistance of neuroblastoma cells to doxorubicin-induced apoptosis (Shang *et al.*, 2010). Thus, it has been suggested that DUSP26 may be a novel therapeutic target for treating cancer.

Apart from MAPKs such as extracellular signal-related kinases (ERKs), c-Jun N-terminal kinase (JNK) and p38, additional substrates for DUSP26 have been identified. In PC12 cells the overexpression of DUSP26 reduced Akt phosphorylation at Ser473 (Wang *et al.*, 2008) and DUSP26 inhibited cell growth in response to epidermal growth factor (EGF) by decreasing the EGF receptor (EGFR) level *via* down-regulation of the Akt pathway and Wilms' tumour gene product (WT1). This suggests that DUSP26 is involved in cell differentiation of PC12 cells in response to nerve growth factor (NGF) and EGF through the regulation of PI3K/Akt signalling. Furthermore, DUSP26 is also associated with cell adhesion and intracellular transport (Tanuma *et al.*, 2009). DUSP26 binds to a subunit of the microtubule-directed motor protein complex KIF3 and thus dephosphorylates Kap3, which may be critical for transporting β-catenin/N-cadherin to the plasma membrane.

In this study, we determined crystal structures of the catalytic domain of DUSP26 (DUSP26-C) and its catalytically inactive mutant DUSP26-C (C152S) at 1.67 and 2.20 Å resolution, respectively. The high-resolution crystal structures of DUSP26-C showed a novel dimeric quaternary structure formed by extensive swapping of the C-terminal domain, although they share a fundamentally similar structural topology with other DUSPs. Structural alignment between DUSP26 and other DUSPs revealed an unusual active-site structure of DUSP26-C that substantially deviates from canonically active DUSP conformations. In addition, the structural identification of two prominent gaps between the protein tyrosine phosphate-binding loop (PTP-loop) and its surrounding loops may provide good targets for the rational design of DUSP26-targeted anticancer drugs.

2. Methods

2.1. Cloning, expression and purification

The region encoding DUSP26-C (residues 61–211) was subcloned from the human DUSP26 gene (Invitrogen, Carlsbad, California, USA) into the expression vector pCR2.1 TOPO as a fusion with an N-terminal His tag and a TEV protease cleavage site. Selenomethionine (SeMet) substituted DUSP26-C was produced using a cell-free protein-synthesis system (Kigawa *et al.*, 2004; Matsuda *et al.*, 2007). DUSP26-C was purified by affinity chromatography on a 5 ml HisTrap column and size-exclusion chromatography on a HiLoad 16/60 Superdex 75 column (GE Healthcare, Little Chalfont, England). The HiLoad 16/60 Superdex 75 column was equilibrated with 20 m*M* Tris–HCl buffer pH 8.0 containing 300 m*M* NaCl and 2 m*M* DTT, and the protein was purified to homogeneity and concentrated to 1.7 mg ml^{-1} using a

Table 1
Data-collection and refinement statistics.

Values in parentheses are for the highest resolution shell. All measured data were included in structure refinement.

Data set	DUSP26-C	λ_1 MAD Se (peak)	λ_2 MAD Se (edge)	λ_3 MAD Se (remote)	DUSP26-C (C152S)
Data collection					
Wavelength (Å)	0.9724	0.9760	0.9794	0.9642	1.0
Space group	*C*2				$P2_12_12_1$
Unit-cell parameters					
a (Å)	80.72				82.60
b (Å)	40.18				82.78
c (Å)	49.94				91.72
α (°)	90.00				90.00
β (°)	110.35				90.00
γ (°)	90.00				90.00
Resolution (Å)	50–1.67	50–2.00	50–2.00	50–1.97	40–2.20
Total reflections	59619	40862	41799	41773	265821
Unique reflections	17046	9848	9711	9967	31803
Completeness (%)	96.9 (77.7)	94.0 (63.7)	94.0 (63.7)	91.8 (54.5)	98.3 (90.2)
Multiplicity	3.5 (2.3)	4.1 (2.8)	4.3 (2.7)	4.2 (2.2)	8.4 (5.6)
$R_{\rm merge}$† (%)	5.4 (13.4)	9.8 (25.4)	10.3 (25.6)	11.1 (27.7)	6.1 (27.7)
$\langle I/\sigma(I)\rangle$	22.2 (7.5)	11.7 (3.9)	12.1 (3.8)	10.8 (2.9)	10.1 (2.6)
Refinement					
No. of reflections	16221				31751
No. of atoms	1196				4866
$R_{\rm cryst}/R_{\rm free}$‡ (%)	17.2/21.2				20.4/26.6
R.m.s. deviations from ideal geometry					
Bond lengths (Å)	0.009				0.022
Bond angles (°)	1.50				1.88
Impropers (°)	0.93				1.75
Dihedrals (°)	22.90				16.86
Temperature factors (Å^2)					
Protein	16.1				43.1
Main-chain atoms	11.7				36.4
Side-chain atoms and waters	19.2				45.3
Ramachandran plot					
Favoured (%)	98.6				96.2
Allowed (%)	1.4				3.6

† $R_{\rm merge} = \sum_{hkl}\sum_i |I_i(hkl) - \langle I(hkl)\rangle| / \sum_{hkl}\sum_i I_i(hkl)$, where $I_i(hkl)$ is the intensity of the *i*th measurement of an equivalent reflection with indices *hkl*. ‡ The $R_{\rm free}$ value was calculated using 5% of the data.

Centricon filter unit (Millipore, Billerica, Massachusetts, USA). The catalytically inactive mutant DUSP26-C (C152S) was subcloned into the pET21a vector and expressed in *Escherichia coli* strain BL21(DE3)RIL. The cells were grown at 303 K after induction with 0.1 m*M* IPTG for 6 h. The cells were harvested and sonicated with lysis buffer consisting of 20 m*M* HEPES–NaOH pH 7.0, 300 m*M* NaCl, 10 m*M* β-mercaptoethanol, 10%(*v*/*v*) glycerol. After cell lysis, the His-tagged protein was purified by nickel-affinity chromatography and Superdex 75 (GE Healthcare) gel-filtration chromatography. The purified mutant protein was dialyzed against a buffer consisting of 20 m*M* HEPES–NaOH pH 7.0, 50 m*M* NaCl, 1 m*M* DTT. Finally, the mutant protein was concentrated to 10 mg ml^{-1} for use in crystallization.

2.2. Crystallization and data collection

Crystallization of DUSP26-C and DUSP26-C (C152S) was performed at 293 K using the sitting-drop vapour-diffusion and microbatch methods, respectively. Initial crystallization was carried out using commercial screening kits (Hampton Research, Aliso Viejo, California, USA). DUSP26-C crystals were obtained in a drop composed of 0.5 µl protein solution mixed with 0.5 µl reservoir solution consisting of 0.1 *M* HEPES–NaOH pH 7.5, 0.8 *M* potassium sodium tartrate tetrahydrate. DUSP26-C (C152S) crystals were grown by mixing 1.3 µl protein solution (10 mg ml^{-1}) with an equal volume of reservoir solution consisting of 0.1 *M* sodium cacodylate pH 6.5, 0.2 *M* calcium acetate hydrate, 18% PEG 8000. After 5 d, the DUSP26-C (C152S) crystals had grown to their full size.

Multi-wavelength anomalous dispersion (MAD) data for DUSP26-C were collected on beamline BL26B1 at the SPring-8 synchrotron facility, Harima, Japan. The wavelengths for Se-atom MAD data collection were selected on the basis of a crystal fluorescence scan corresponding to the *K* absorption edge of an Se atom. The MAD data set was collected at three wavelengths: 0.9760 Å (peak), 0.9794 Å (edge) and 0.9642 Å (remote). The crystal in the droplet was transferred to a cryosolution consisting of the mother liquor supplemented with 20%(*v*/*v*) ethylene glycol for 1 min and was then flash-cooled in a nitrogen-gas stream at 93 K. The X-ray diffraction data for DUSP26-C were collected to 2.0 Å resolution and were indexed, scaled and merged using the *HKL*-2000 software (Otwinowski & Minor, 1997). The DUSP26-C crystal belonged to space group *C*2, with unit-cell parameters $a = 80.72$, $b = 40.18$, $c = 49.94$ Å, $\alpha = 90.00$, $\beta = 110.35$, $\gamma = 90.00^\circ$. X-ray diffraction data for DUSP26-C (C152S) were collected to 2.2 Å resolution on beamline BL17A at the Photon Factory, Tsukuba, Japan. Diffraction data were processed and scaled using the programs *MOSFLM* (Leslie, 1999) and *SCALA* (Evans, 2006). The DUSP26-C (C152S) crystal belonged to space group $P2_12_12_1$, with unit-cell parameters $a = 82.60$, $b = 82.78$, $c = 91.72$ Å, $\alpha = \beta = \gamma = 90.00^\circ$.

2.3. Structure solution and refinement

Phasing of the DUSP26-C data was carried out using the MAD method. The positions of the Se atoms in the asymmetric unit and the initial phases were calculated using *SOLVE* (Terwilliger & Berendzen, 1999) and the phases were improved using *RESOLVE* (Terwilliger & Berendzen, 1999), yielding an overall figure of merit (FOM) of 0.73. Model building of DUSP26-C was performed using *O* (Jones *et al.*, 1991). Structure refinement of DUSP26-C was performed

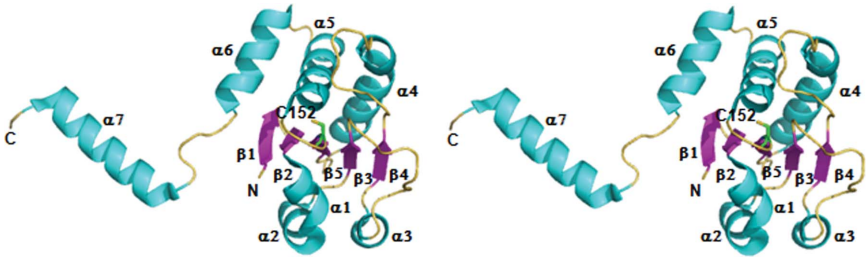

Figure 1
Overall structure of the DUSP26-C monomer. Stereo image of a ribbon model of the monomeric DUSP26-C structure. The Cys152 residue is shown as a stick model. Secondary-structural elements are labelled.

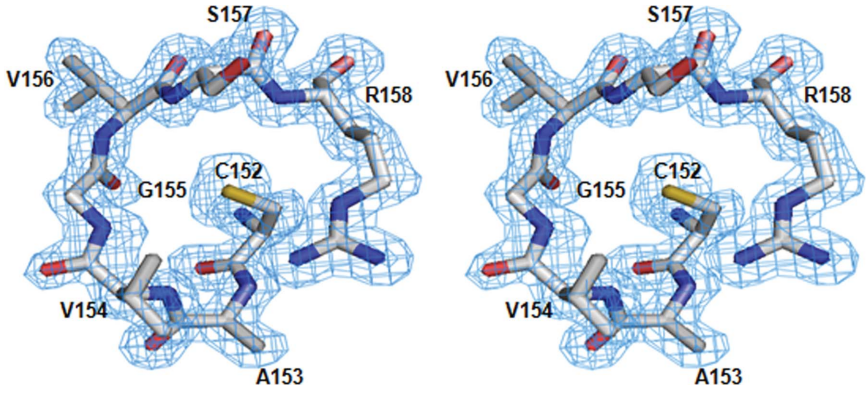

Figure 2
Stereo image of the electron-density map at the active site. The σ_A-weighted $2mF_o - DF_c$ electron-density map (1.67 Å resolution, contoured at the 1.6σ level) for the active-site residues of the PTP-loop of DUSP26-C is shown. Residues are drawn as sticks with C atoms in grey, N atoms in blue and O atoms in red.

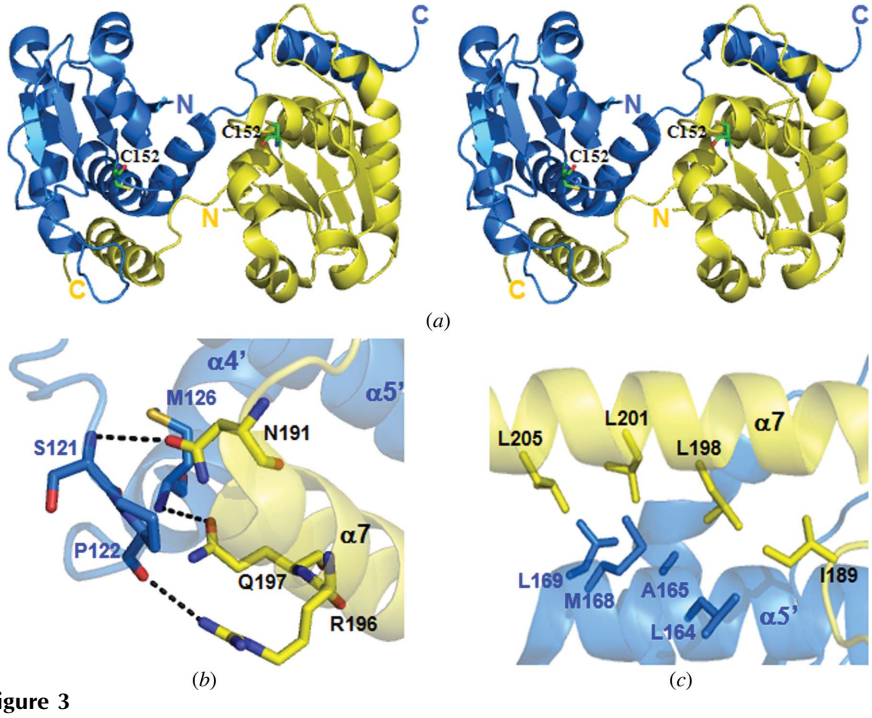

Figure 3
Structure of the C-terminal domain-swapped dimer of DUSP26-C. (*a*) Stereo image of a ribbon model of the dimeric DUSP26-C structure. Chains *A* and *B* of DUSP26-C are coloured blue and yellow, respectively. The N- and C-termini are labelled. (*b*, *c*) Dimeric interfaces between subunits. The hydrogen-bonding interactions in DUSP26-C are indicated as dotted lines.

using *CNS* (Brünger *et al.*, 1998) with the higher resolution data set (1.67 Å resolution) collected on beamline 22ID at the Advanced Photon Source (APS), Argonne National Laboratory, Chicago, Illinois, USA. The structure of the DUSP26-C (C152S) mutant was determined by molecular replacement using the wild-type DUSP26-C structure as a search model. Phases were determined using *Phaser*. The *CCP*4 suite (Winn *et al.*, 2011) placed two dimers of DUSP26-C (C152S) in the asymmetric unit. The interactive manual model was built using *Coot* (Emsley *et al.*, 2010) and *O* (Jones *et al.*, 1991) and was refined using *PHENIX* (Adams *et al.*, 2010). The stereochemical quality of the final model was assessed using *PROCHECK* (Laskowski *et al.*, 1993) and *WHAT IF* (Vriend, 1990). Statistics of data collection and refinement and of the Ramachandran plot are summarized in Table 1. Figures were drawn using *PyMOL* (http://www.pymol.org). Atomic coordinates and experimental structure factors for DUSP26-C and DUSP26-C (C152S) at 1.67 and 2.20 Å resolution have been deposited in the PDB with accession codes 2e0t and 4b04, respectively.

2.4. Phosphatase-activity measurements

In the *para*-nitrophenyl phosphate (pNPP) assay, DUSP26-C, DUSP26-C (C152S) and VH1-related DUSP (VHR; residues 1–185) proteins of 250–1500 pmol ml^{-1} were incubated at 310 K for 30 min in a reaction buffer consisting of 50 m*M* bis-tris pH 6.0, 100 m*M* NaCl, 2 m*M* DTT, 20 m*M* pNPP. The reaction was stopped by the addition of 0.1 *N* NaOH and the hydrolysis of pNPP was determined by measuring the absorbance at 450 nm. In the 6,8-difluoro-4-methylumbelliferyl phosphate (DiFMUP) assay, DUSP26-C, DUSP26-C (C152S) and VHR of 5500 pmol ml^{-1} were reacted with 500 µ*M* DiFMUP in a reaction buffer consisting of 50 m*M* bis-tris pH 6.0, 1 m*M* DTT at room temperature. Fluorescence was measured in a fluorescence microplate reader using excitation at 355 nm and emission detection at 460 nm.

2.5. Acidic native gel electrophoresis and chemical cross-linking

Because of the basic pI (pI = 9.25) of DUSP26-C at neutral pH, native gel electrophoresis was performed under acidic conditions in combination with reversed polarity. 60 µg DUSP26-C protein was mixed with 5× dissolving buffer [37.2%(*v*/*v*) glycerol, 64 m*M* potassium acetate pH 6.8, 0.05% methyl green] and loaded onto 20% polyacrylamide gradient gels. Electrophoresis was performed in running buffer consisting of 350 m*M* *β*-alanine and 140 m*M* acetic acid pH 4.3 at 150 V for 90 min at 277 K followed by Coomassie Blue staining. For the cross-linking experiment, 30 µg of DUSP26C and DUSP26-C (C152S) were incubated in 20 m*M* HEPES–NaOH pH 6.5, 50 m*M* NaCl, 1 m*M* DTT with 0.1% glutaraldehyde at 298 K for 30 min. The reaction mixture was analyzed by SDS–PAGE.

2.6. Isothermal titration calorimetry (ITC) measurements

ITC measurements were performed at 298 K in a buffer consisting of 20 m*M* HEPES–NaOH pH 6.5, 50 m*M* NaCl, 1 m*M* DTT using an Auto-iTC$_{200}$ system at Korea Basic Science Institute. Protein samples at 450 µ*M* were titrated into the calorimeter cell containing the buffer using 2 µl injections. The ITC data were analyzed using the MicroCal *Origin* software.

3. Results and discussion

3.1. Overall structure of the monomer

For structural studies, we chose an N-terminally truncated construct of DUSP26 encompassing residues 61–211 (DUSP26-C); we were unable to purify full-length DUSP26 owing to its insolubility. Because of its low pK_a value, the active-site cysteine of PTPs is susceptible to oxidation. An approach used to overcome this limitation is to mutate the active-site cysteine to serine, which does not affect the intact structure or substrate binding. Therefore, we crystallized both wild-type and C152S mutant forms of DUSP26-C. The crystal structures of DUSP26-C and its catalytically inactive mutant DUSP26-C (C152S) have been determined and refined to 1.67 and 2.2 Å resolution, respectively (Table 1). The structure of DUSP26-C was solved in space group *C*2 using the MAD technique with SeMet-substituted protein. The structure of DUSP26-C (C152S) was subsequently solved in space group $P2_12_12_1$ by molecular replacement using the DUSP26-C structure as a search model. DUSP26-C and DUSP26-C (C152S) both crystallized as domain-swapped dimers with essentially identical structures, with a root-mean-square deviation (r.m.s.d.) of 0.55 Å. The DUSP26-C monomer has a central twisted five-stranded *β*-sheet (*β*1–*β*5) surrounded by seven *α*-helices (Fig. 1). One side of the *β*-sheet is covered by three *α*-helices (*α*1–*α*3), and the other side is covered by three *α*-helices (*α*4–*α*6) from one monomer and an *α*-helix (*α*7′) from the other monomer. A search for homologous structures using the program *DALI* (Holm & Sander, 1993) identified several DUSP-family members, including DUSP27 (PDB entry 2y96; *Z*-score = 21.0; Lountos *et al.*, 2011), DUSP13 (PDB entry 2pq5; *Z*-score = 19.5; Structural Genomics Consortium, unpublished work) and VHR (PDB entry 1vhr; *Z*-score = 19.1; Yuvaniyama *et al.*, 1996). When the structure of DUSP26-C was aligned with those of DUSP27 and VHR, 111 and 110 of the 150 DUSP26-C residues could be superimposed with

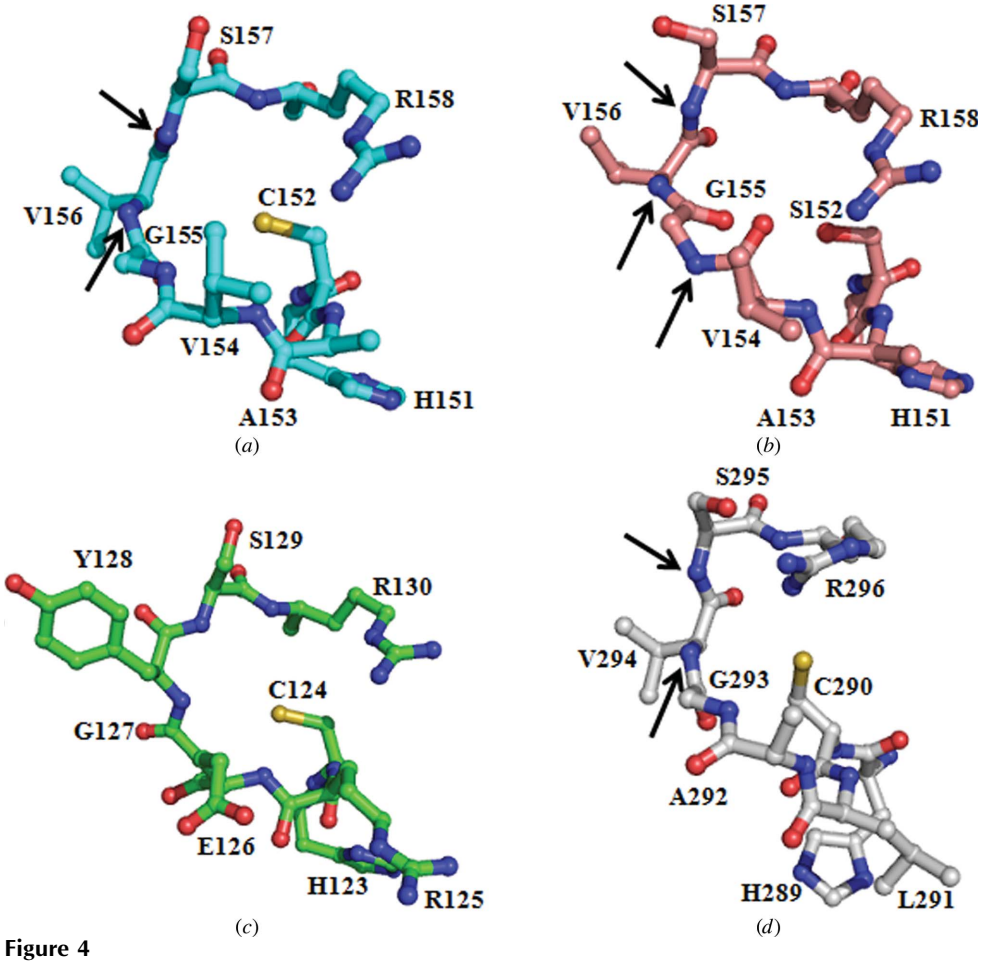

Figure 4
Comparison of the PTP-loop conformation in (*a*) DUSP26-C, (*b*) the DUSP26-C (C152S) mutant, (*c*) VHR (PDB entry 1vhr) and (*d*) MKP-4 (PDB entry 3lj8; Jeong *et al.*, 2011). The black arrow highlights the backbone amide atoms that are flipped away from the active site.

r.m.s.d.s of 0.71 and 0.74 Å, respectively. Thus, the overall global fold of the DUSP26-C monomer is highly similar to those of DUSP27 and VHR, except that the C-terminal α7 helix projects away from the catalytic core in DUSP26-C. In DUSP26-C, residues 61–210 in chain *A* were clearly visible in the electron-density maps. In DUSP26-C (C152S), chains *A* and *B* are well ordered throughout the structure, whereas the electron density for residues 97–100 in chain *C* and residues 75 and 97–99 in chain *D* is poorly defined. The quality of the electron-density maps for the active-site residues is shown in Fig. 2.

3.2. C-terminal domain-swapped dimer

There is one molecule in the asymmetric unit of the DUSP26-C crystal, giving a V_M value of 2.24 Å^3 Da^{-1} and an approximate solvent content of 45%. DUSP26-C forms a dimer with a symmetry-related molecule *via* C-terminal domain-swapping (Fig. 3*a*). There are four molecules of DUSP26-C (C152S) in the asymmetric unit, in which two dimers are related by twofold noncrystallographic symmetry in the same manner. It is noteworthy that the same domain-swapped dimer was found in the distinct crystals of DUSP26-C and DUSP26-C (C152S) despite the difference in the space groups of the crystals. A novel structural feature of DUSP26-C that distinguishes it from the other DUSPs lies in the orientation of the C-terminal α7 helix (residues 192–207). In the monomeric VHR the C-terminal α7 helix is packed against the catalytic core domain to form a four-helix bundle (Yuvaniyama *et al.*, 1996). In contrast, the equivalent C-terminal α7 helix in DUSP26-C is flipped in the opposite direction, projecting away from the catalytic core. Consequently, the C-terminal α7 helix of one monomer forms a four-helix bundle with α-helices of the other monomer. Hence, the dimerization of DUSP26-C is mediated through extensive crossover of the C-terminal α7 helix (Fig. 3*a*). The α7-helix residues of each monomer form a dimeric interface with the residues of the β4′–α4′ loop of the counterpart monomer through a series of intermolecular hydrogen bonds. The representative hydrogen bonds include Ser121···Asn191, Pro122···Arg196 and Met126···Gln197 (Fig. 3*b*). Furthermore, the domain-swapped dimerization is stabilized by extensive intersubunit hydrophobic interactions between the α7 helix of one monomer and the α5′ helix of the other monomer (Fig. 3*c*).

The domain-swapped dimeric structure of DUSP26-C is reminiscent of those of *Vaccinia virus* H1 (VH1) phosphatase (Koksal *et al.*, 2009), *Variola virus* H1 phosphatase (Phan *et al.*, 2007) and DUSP27 (Lountos *et al.*, 2011). Although these molecules also have domain-swapped dimeric structures, the dimerization is mediated by the swapping of an N-terminal domain (α1 helix). This sharply contrasts with the DUSP26-C dimeric structure, which is formed by C-terminal domain-swapping. Two catalytic cysteines within the dimer are spaced ∼40 Å away from each other on the surfaces of VH1 and DUSP27. In comparison, the two catalytic cysteines in the DUSP26 dimer are more closely positioned (separated by ∼19 Å) than those in VH1 and DUSP27. In addition, the dimeric interfaces of DUSP26-C and DUSP26-C (C152S) bury ∼36% (∼2960 Å^2 from each monomer) and ∼37% (∼3659 Å^2) of the total monomeric surface area, respectively. These values are larger than or comparable to those of the biologically active dimers of VH1 (∼24%, 2101 Å^2) and human DUSP27 (∼37%, 3920 Å^2), suggesting that the dimeric structures of DUSP26-C and DUSP26-C (C152S) are not artifacts of crystallization.

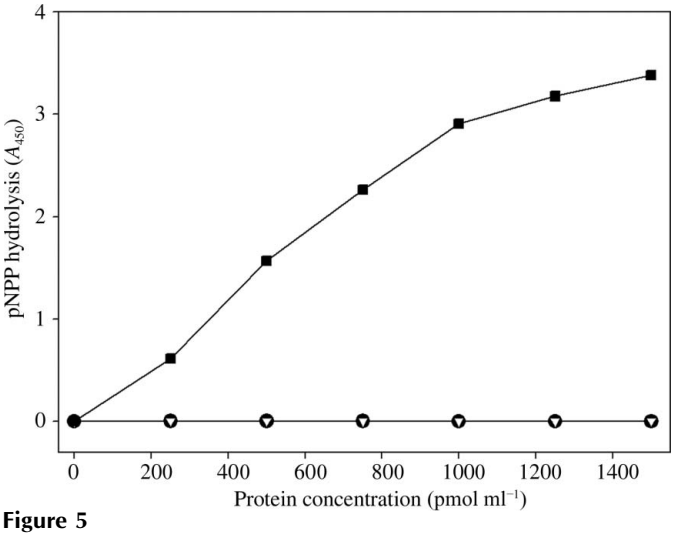

Figure 5
Phosphatase-activity measurements for DUSP26-C using pNPP as a substrate. The phosphatase activities of DUSP26-C (filled circles), DUSP26-C (C152S) (inverted triangles) and VHR (filled squares) were determined by the effective hydrolysis of the phosphatase substrate pNPP at different protein concentrations.

3.3. Active-site conformation and phosphatase activity

The active site of cysteine-based PTPs consists of the PTP-loop [consensus sequence HC*xx*G*xx*RS(T)] and an aspartate which acts as a general acid (Denu & Dixon, 1998). The common active-site conformation can be defined by the direction of the side chain of the active-site cysteine, an inward orientation of the backbone amides of the PTP-loop and the proper positioning of the general acid aspartate. The side chain of the active-site cysteine is positioned beneath the PTP-loop. The partially positively charged backbone amides of the PTP-loop and guanidinium group of arginine, directed towards the interior of the PTP-loop, and the α-helix dipole create a positive electrostatic potential (Zhang, 2002). These characteristics contribute not only to lowering the pK_a value of the active-site cysteine (pK_a = 4.5–5.5), which is essential for it to act as an efficient nucleophile, but also to providing a charge-complementary pocket for incoming phosphate-containing substrates (Zhang *et al.*, 1994). The active site of DUSP26-C is composed of the PTP-loop and the general acid residue Asp120. The PTP-loop of DUSP26-C has a conserved consensus motif, His151-Cys-Ala-Val-Gly-Val-Ser-Arg-Ser159, which is part of the loop between the β5 strand and the α5 helix. The catalytic thiol of Cys152, which acts as a nucleophile, is surrounded by the PTP-loop. The general acid residue

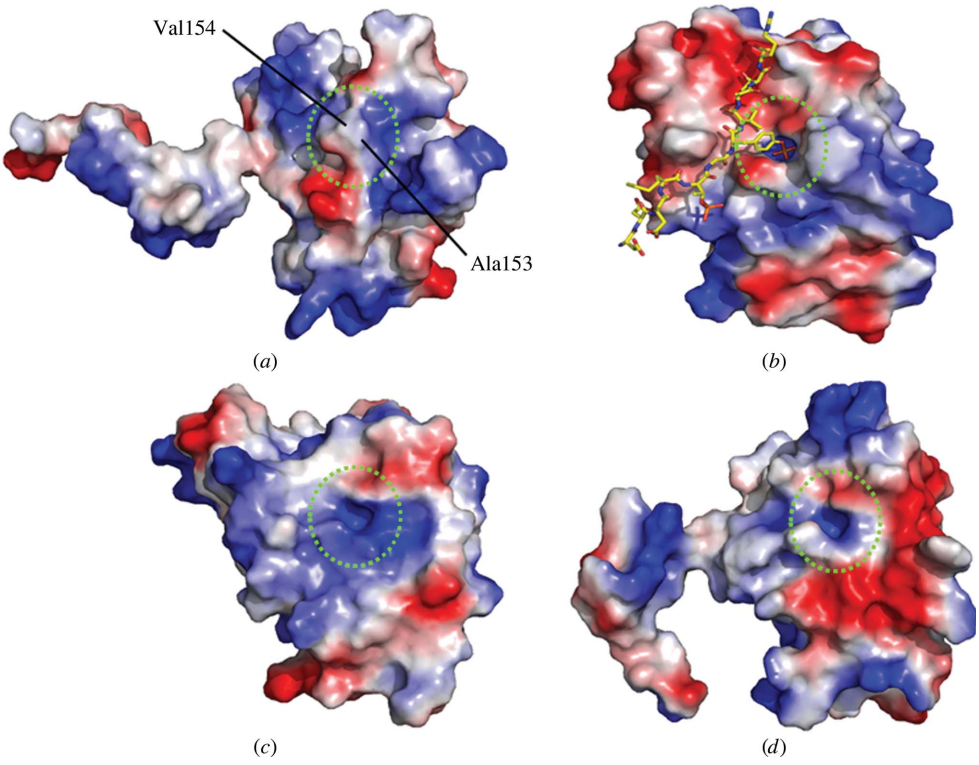

Figure 6
Electrostatic surface representation of the structures of (*a*) the DUSP26-C monomer, (*b*) a VHR–peptide [DDE(Nle)pTGpYVATR; shown as yellow sticks] complex (PDB entry 1j4x; Schumacher *et al.*, 2002), (*c*) VH1 and (*d*) DUSP27. The side chains of Ala153 and Val154 in the PTP-loop of DUSP26-C are labelled. Positively charged regions are depicted in blue and negatively charged region in red. The green dotted circle indicates the location of the substrate-binding pocket of the DUSPs.

Asp120 in DUSP26-C occupies a position similar to that of Asp92 in VHR and forms a hydrogen bond to the side chain of Ser157.

Structural comparison with VHR and MKP-4 revealed that both DUSP26-C and DUSP26-C (C152S) adopt a distorted PTP-loop conformation that significantly deviates from the canonically active structures of other DUSPs (Figs. 4*a* and 4*b*). In VHR, the backbone amide atoms of residues 124–130 and the guanidinium group of Arg130 in the PTP-loop are directed towards the active-site pocket, thereby creating positive electrostatic potential which is critical for the catalytic reaction of the cysteine thiolate anion (Fig. 4*c*). In the PTP-loop, the backbone amide atoms of Val156 and Ser157 in DUSP26-C (Fig. 4*a*) and of Gly155, Val156 and Ser157 in DUSP26-C (C152S) (Fig. 4*b*) are flipped in the opposite direction, projecting away from the active site. As a result, the main-chain dihedral angles of Val156 and Ser157 in DUSP26-C deviate greatly from those of the corresponding residues in canonically active VHR irrespective of the presence of a catalytic cysteine thiolate group. Thus, owing to the resultant improper orientation of the PTP-loop in DUSP26-C, positive electrostatic potential that results in the high reactivity of the catalytic cysteine is not created and the substrate-binding pocket thus shrinks. This distorted PTP-loop conformation of DUSP26-C is analogous to that of inactive MKP-4, in which the backbone amide atoms of Val294 and Ser295 are flipped away from the active site (Fig. 4*d*; Jeong *et al.*, 2011). Camps and coworkers suggested that MKP-4 follows a well known substrate-induced activation mechanism (Camps *et al.*, 1998) in which substrate binding triggers the transition of the PTP-loop from an inactive to an active conformation. Indeed, the isolated catalytic domain of MKP-4 has minimal catalytic activity, whereas its full catalytic activity is induced when the N-terminal MKB domain binds to MAPK. Taken together, this suggests that DUSP26-C adopts a catalytically inactive conformation of the PTP-loop. To confirm this, we performed a phosphatase activity assay on DUSP26-C using pNPP as a substrate (Fig. 5). VHR and the catalytically inactive mutant DUSP26-C (C152S) were used as positive and negative controls, respectively, to compare enzyme activity. DUSP26-C exhibited no phosphatase activity at various concentrations, whereas VHR was catalytically active towards pNPP. These enzyme-activity assay results are highly consistent with our crystal structure of DUSP26-C.

Since the K_m values of PTPs for DiFMUP are much lower than for pNPP, the DiFMUP assay has been widely used as a more sensitive method than the pNPP assay for measuring the catalytic activities of DUSPs (Welte *et al.*, 2005). Although the pNPP assay showed no catalytic activity in the concentration range used, the DiFMUP assay showed that DUSP26-C has a basal level of intrinsic catalytic activity but the catalytically inactive mutant DUSP26-C (C152S) does not (Supplementary Fig. S1[1]). This observed level of phosphatase activity was comparable to that of the catalytic domain of MKP-4 in the absence of substrate (data not shown). As for the MKP-4 catalytic domain, the catalytic activity of DUSP26-C was too low to detect using the pNPP assay, but it is clear that DUSP26-C possesses a basal level of intrinsic catalytic activity. Thus, it is possible that the DUSP26-C monomer is catalytically active.

3.4. Comparison of the substrate-binding site

Despite the high degree of structural similarity between DUSP26-C and other DUSPs, including VH1, DUSP27 and VHR, the distribution of electrostatic potential and the

[1] Supplementary material has been deposited in the IUCr electronic archive (Reference: MH5076). Services for accessing this material are described at the back of the journal.

topographical details of the molecular surfaces are quite different (Fig. 6). Overall, the surface-charge patterns differ significantly among the DUSPs. The negatively charged residues are predominantly located in the top half of the VHR molecule (Fig. 6*b*) and (to a lesser extent) of DUSP27 (Fig. 6*d*), whereas positively charged residues are localized near the centre of the DUSP26-C (Fig. 6*a*) and VH1 (Fig. 6*c*) molecules. In the DUSP26-C molecule there is a long hydrophobic patch exposed by the C-terminal α-helix that mediates the intermolecular interaction for the domain-swapping. Another unusual feature of the electrostatic surface of DUSP26-C is observed in its substrate-binding site. Most DUSPs, including VH1, DUSP27 and VHR, possess a positively charged substrate-binding pocket of ~6 Å in depth into which the phosphoryl group of a cognate substrate can fit. However, this characteristic substrate-binding pocket is not observed in the DUSP26-C structure because entry to the substrate-binding pocket is prevented by the hydrophobic side chains of Ala153 and Val154 in the PTP-loop (Fig. 6*a*). As a result, the catalytic cysteine located at the bottom of the substrate-binding pocket cannot access the phosphoryl group of the cognate substrate. This finding is consistent with the observation that DUSP26-C shows no phosphatase activity.

3.5. Structural identification of unique gaps between the PTP-loop and its surrounding loops

Structural superimposition of the domain-swapped DUSP26-C dimer with the VHR monomer showed that the swapped $\alpha7'$ helix from the counterpart monomer in the DUSP26-C dimer was well aligned with the VHR $\alpha7$-helix (Fig. 7*a*). This finding suggests that, similar to VHR, the DUSP26-C monomer can adopt a 'folded-back' conformation in which the C-terminal $\alpha7$-helix is not domain-swapped. However, a detailed comparison with the active conformation of VHR revealed significant structural differences in the two loops surrounding the PTP-loop. Firstly, one of the largest conformational differences between DUSP26-C and VHR was found in the conformation of the $\alpha6'$–$\alpha7'$ loop spanning residues 185–191 (as highlighted by the red dotted circle), which corresponds to the hinge region of the swapped C-terminal domain of DUSP26-C (referred to as the swapping hinge loop). As shown in the VHR structure, the active PTP-loop conformation of DUSPs was maintained by hydrogen bonds between the PTP-loop and the surrounding loops. The analogous surrounding $\alpha6$–$\alpha7$ loop of VHR formed an extensive hydrogen-bond network with the PTP-loop (Fig. 7*b*) involving Arg158···Glu126, Arg158···Gly127, Gly161···Tyr128, Gly161···Ser129 and Asn163···Ser129 hydrogen bonds. These tight interactions between the PTP-loop and the surrounding $\alpha6$–$\alpha7$ loop may play a structural role in stabilizing the active PTP-loop conformation of VHR. However, all corresponding hydrogen bonds between the PTP-loop and swapping hinge loop were completely abolished in DUSP26-C (Fig. 7*c*). Because of the absence of such interactions with the swapping hinge loop, the PTP-loop of DUSP26-C was destabilized and thus assumed an inactive noncanonical conformation. Secondly, another significant difference between DUSP26-C and the active forms of other DUSPs was found in the interaction between the PTP-loop and its surrounding loop $\beta3$–$\alpha3$ (residues 94–105; Figs. 8*a* and 8*b*). The C^{α}-atom positions of the $\beta3$–$\alpha3$ loop of DUSP26-C deviate by the large magnitude of ~10 Å from the equivalent

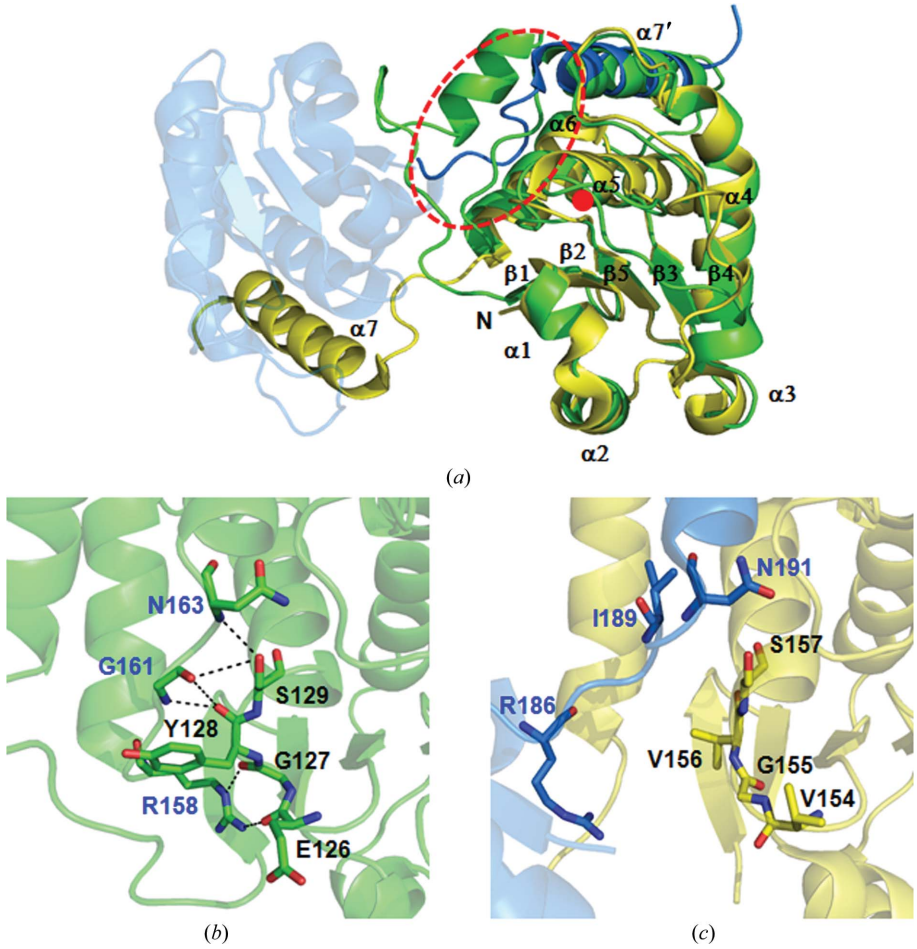

Figure 7
(*a*) Superposition of monomeric VHR (green) onto chain *B* (yellow) of the DUSP26-C dimer. The red dotted circle highlights the large conformational difference in the $\alpha6$–$\alpha7$ loop between DUSP26-C and VHR. The red dot indicates the location of the C^{α} atom of the catalytic cysteine. (*b*) Hydrogen-bonding interactions between the PTP-loop and the surrounding $\alpha6$–$\alpha7$ loop in VHR. Residues in the PTP-loop (Glu126, Gly127, Tyr128 and Ser129) form hydrogen bonds to residues in the $\alpha6$–$\alpha7$ loop. Hydrogen bonds are indicated by dotted lines. (*c*) All equivalent hydrogen bonds in DUSP26 are disrupted upon dimerization according to the structure.

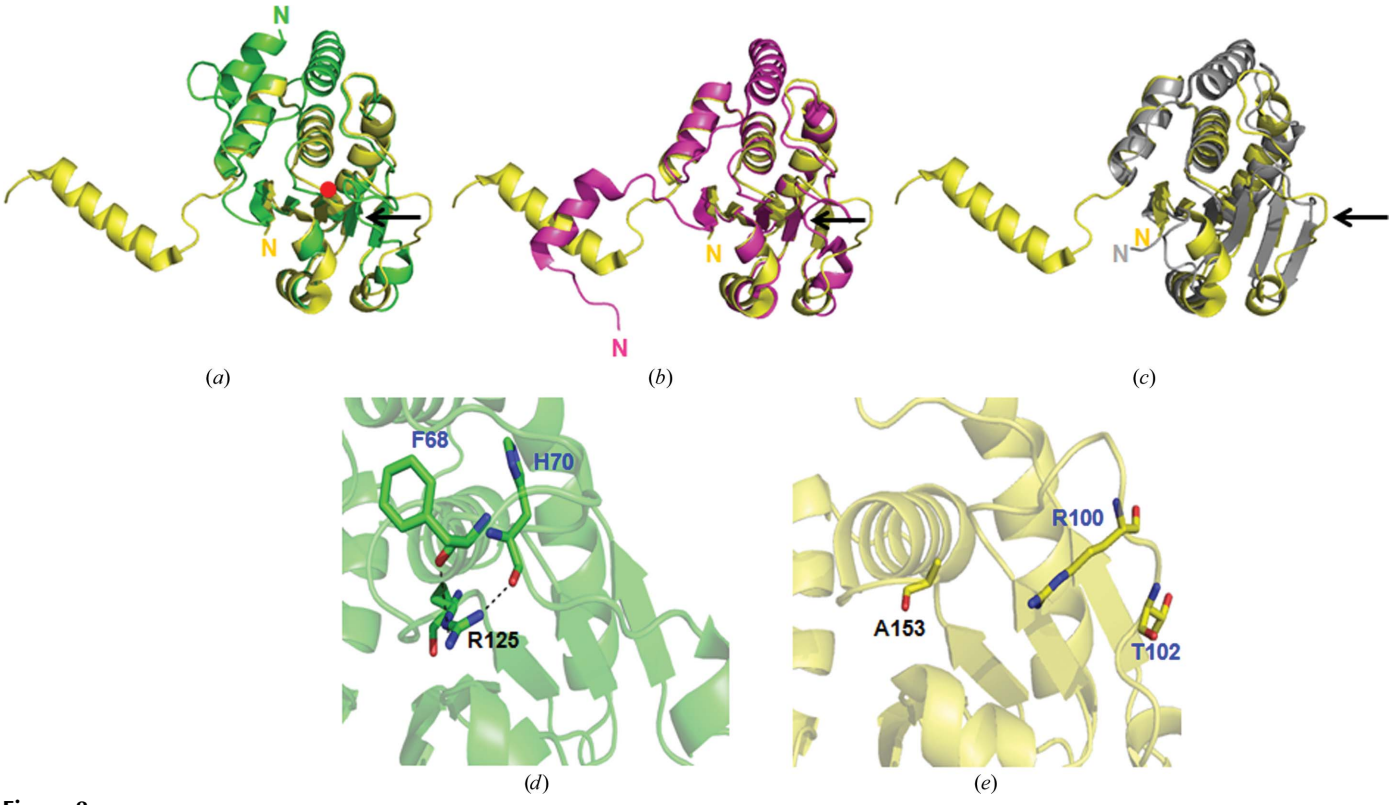

Figure 8
Superposition of (*a*) VHR (green), (*b*) DUSP27 (magenta) and (*c*) MKP-4 (grey) onto chain *B* of DUSP26-C (yellow). The black arrow highlights the large conformational difference in the $\beta3$–$\alpha3$ loop between DUSP26-C and other DUSPs. The red dot indicates the location of the C^{α} atom of the catalytic cysteine. (*d*) Hydrogen bonds between the PTP-loop and the surrounding $\beta3$–$\alpha3$ loop in VHR. Hydrogen bonds are indicated by dotted lines. (*e*) Both equivalent hydrogen bonds in DUSP26-C are disrupted upon dimerization according to the structure.

positions in VHR and DUSP27 (as highlighted by the black arrows). However, structural alignment of DUSP26-C and the inactive MKP-4 showed no such substantial conformational differences in the corresponding region. The residues in the $\beta3$–$\alpha3$ loop of DUSP26-C occupy essentially the same site as that filled by the equivalent residues in the $\beta4$ strand of MKP-4 (Fig. 8*c*), indicating that the DUSP26-C structure is most likely to resemble the inactive conformation of MKP-4. In VHR, the main-chain carbonyl O atoms of Phe68 and His70 in the analogous surrounding loop form two hydrogen bonds to the Arg125 side chain in the PTP-loop (Fig. 8*d*), stabilizing the active PTP-loop conformation of VHR. In contrast, both hydrogen bonds between the corresponding residues are impaired in DUSP26-C (Fig. 8*e*).

Taken together, structural comparison of DUSP26-C with the active forms of DUSPs revealed two significant gaps between the outer rim of the PTP-loop and its surrounding loops (the $\alpha6$–$\alpha7$ and $\beta3$–$\alpha3$ loops) in DUSP26-C. Such gaps can be used as allosteric binding sites to prevent conversion of DUSP26-C to the active conformation in a similar manner as observed in MKP-4 (Jeong *et al.*, 2011). Targeting binding sites other than the active site using small-molecule compounds may result in greater specificity as well as higher affinity relative to other PTPs. Thus, specific compounds targeting the two significant gaps in DUSP26-C can be designed based on the high-resolution crystal structure. In summary, the identification of unique allosteric binding sites in the DUSP26 structure may facilitate structure-based design of DUSP26-targeted anticancer drugs.

3.6. Dimerization of DUSP26

To determine whether DUSP26-C exists as a dimer in solution, we performed acidic native gel electrophoresis, chemical cross-linking experiments and ITC measurements (Supplementary Fig. S2). Although DUSP26-C eluted as a single peak at an apparently monomeric position on the size-exclusion chromatogram (data not shown), acidic native gel electrophoresis, cross-linking experiments and ITC measurements indicated that an equilibrium exists between dimeric and monomeric DUSP26-C proteins in solution. According to acidic native gel electrophoresis (Supplementary Fig. S2*a*) and cross-linking experiments (Supplementary Fig. S2*b*), the DUSP26-C proteins appeared as two discrete bands with molecular masses corresponding to a monomer (the expected molecular weight of the monomer was 18 087 Da) and a dimer, indicating the existence of a mixture of monomer and dimer in solution. In particular, the ITC measurements clearly showed endothermic peaks indicative of dissociation of the homodimer into monomers, with a dissociation constant (K_d) of 38 μM, confirming the presence of the dimer in solution (Supplementary Fig. S2*c*). Although the high protein concentration of DUSP26-C may shift the equilibrium towards the dimer during crystallization, it remains to be determined

which factor induces the dimerization of DUSP26-C in solution.

Dimerization is a physiologically significant mechanism for controlling the catalytic activity and substrate specificity of classical PTPs (Wiesmann *et al.*, 2004). However, little is known regarding the functional role of dimerization in DUSPs, which are generally assumed to function as monomers. Although most DUSP structures solved to date are monomers, domain-swapped dimerization has been observed in several DUSPs such as VH1, *Variola virus* H1 and human DUSP27. In particular, dimerization has been shown to be essential for the catalytic activities of VH1 and laforin (Koksal & Cingolani, 2011; Liu *et al.*, 2006). In this study, we present the first structure of an inactive dimeric DUSP with C-terminal domain-swapping. Structural comparison with active forms of other DUSPs revealed that unlike other DUSP dimers, DUSP26-C adopts a catalytically inactive noncanonical PTP-loop conformation, which is consistent with the phosphatase-activity assay results showing that DUSP26-C has no catalytic activity. Interestingly, a notable difference between inactive DUSP26-C and active forms of DUSPs was observed at the hinge region of a swapped C-terminal domain which constitutes part of the dimeric interface (Fig. 7). This finding suggests that the conversion of DUSP26-C to an inactive conformation results from a significant conformational change arising from domain-swapping upon dimerization. However, we cannot exclude the possibility that the unusually long N-terminal region (residues 1–60), which is not present in the DUSP26-C structure, is associated with regulation of catalytic activity or with dimerization. Thus, further structure studies of full-length DUSP26 containing its N-terminal residues are required in order to elucidate the molecular mechanism of DUSP26 regulation.

4. Conclusion

In summary, we determined the high-resolution crystal structures of DUSP26-C and DUSP26-C (C152S). The 1.67 Å resolution structure of DUSP26-C presented here, which is the highest resolution structure reported for a human atypical DUSP with the exception of SKRP-1 (Wei *et al.*, 2011), showed a novel dimeric structure with C-terminal domain-swapping, providing a unique view of the DUSP catalytic site. In combination with the results of a phosphatase-activity assay, structural comparison with other DUSPs revealed that the DUSP26-C dimer assumes an inactive PTP-loop conformation that is completely different from those of other active forms of DUSPs. Additionally, we identified unique structural characteristics of DUSP26-C that can be used as additional binding sites for allosteric regulation. Thus, the crystal structure of DUSP26-C may provide a useful template for exploring the selectivity and efficacy of enzyme regulation and may contribute to the development of anticancer therapeutic agents.

The authors are grateful to the beamline staff of the Southeast Regional Collaborative Access Team (SER-CAT) at the 22-ID beamline at the Advanced Photon Source (APS), Argonne National Laboratory. Use of the APS was supported by the US Department of Energy, Office of Science, Office of Basic Energy Sciences under Contract No. W-31-109-Eng-38. We also thank Drs Kawamoto and Yamamoto for the use of BL26B1 at SPring-8 and Ji-Hyang Ha and Dr Mi-kyung Yoon for ITC measurements. This work was supported by National Research Foundation of Korea (NRF) grants funded by the Korean government (MEST; Nos. 2011-0016011 and 2011-0030027). This study was supported by the RIKEN Structural Genomics/Proteomics Initiative (RSGI) and the National Project on Protein Structural and Functional Analyses, Ministry of Education, Culture, Sports, Science and Technology of Japan.

References

Adams, P. D. *et al.* (2010). *Acta Cryst.* D**66**, 213–221.
Almo, S. C. *et al.* (2007). *J. Struct. Funct. Genomics*, **8**, 121–140.
Alonso, A., Sasin, J., Bottini, N., Friedberg, I., Friedberg, I., Osterman, A., Godzik, A., Hunter, T., Dixon, J. & Mustelin, T. (2004). *Cell*, **117**, 699–711.
Blaskovich, M. A. (2009). *Curr. Med. Chem.* **16**, 2095–2176.
Brünger, A. T., Adams, P. D., Clore, G. M., DeLano, W. L., Gros, P., Grosse-Kunstleve, R. W., Jiang, J.-S., Kuszewski, J., Nilges, M., Pannu, N. S., Read, R. J., Rice, L. M., Simonson, T. & Warren, G. L. (1998). *Acta Cryst.* D**54**, 905–921.
Camps, M., Nichols, A., Gillieron, C., Antonsson, B., Muda, M., Chabert, C., Boschert, U. & Arkinstall, S. (1998). *Science*, **280**, 1262–1265.
Denu, J. M. & Dixon, J. E. (1998). *Curr. Opin. Chem. Biol.* **2**, 633–641.
Denu, J. M., Stuckey, J. A., Saper, M. A. & Dixon, J. E. (1996). *Cell*, **87**, 361–364.
Emsley, P., Lohkamp, B., Scott, W. G. & Cowtan, K. (2010). *Acta Cryst.* D**66**, 486–501.
Evans, P. (2006). *Acta Cryst.* D**62**, 72–82.
Farooq, A. & Zhou, M. M. (2004). *Cell. Signal.* **16**, 769–779.
Hoffman, B. T., Nelson, M. R., Burdick, K. & Baxter, S. M. (2004). *Curr. Pharm. Des.* **10**, 1161–1181.
Holm, L. & Sander, C. (1993). *J. Mol. Biol.* **233**, 123–138.
Hu, Y. & Mivechi, N. F. (2006). *Mol. Cell. Biol.* **26**, 3282–3294.
Hunter, T. (1995). *Cell*, **80**, 225–236.
Jeong, D. G., Yoon, T. S., Jung, S.-K., Park, B. C., Park, H., Ryu, S. E. & Kim, S. J. (2011). *Acta Cryst.* D**67**, 25–31.
Jones, T. A., Zou, J.-Y., Cowan, S. W. & Kjeldgaard, M. (1991). *Acta Cryst.* A**47**, 110–119.
Kigawa, T., Yabuki, T., Matsuda, N., Matsuda, T., Nakajima, R., Tanaka, A. & Yokoyama, S. (2004). *J. Struct. Funct. Genomics*, **5**, 63–68.
Kim, S. J., Jeong, D. G., Jeong, S.-K., Yoon, T. S. & Ryu, S. E. (2007). *Diabetes*, **56**, 41–48.
Koksal, A. C. & Cingolani, G. (2011). *J. Biol. Chem.* **286**, 14373–14382.
Koksal, A. C., Nardozzi, J. D. & Cingolani, G. (2009). *J. Biol. Chem.* **284**, 10129–10137.
Laskowski, R. A., Moss, D. S. & Thornton, J. M. (1993). *J. Mol. Biol.* **231**, 1049–1067.
Leslie, A. G. W. (1999). *Acta Cryst.* D**55**, 1696–1702.
Liu, Y., Wang, Y., Wu, C., Liu, Y. & Zheng, P. (2006). *J. Biol. Chem.* **281**, 34768–34774.
Lountos, G. T., Tropea, J. E. & Waugh, D. S. (2011). *Acta Cryst.* D**67**, 471–479.
Matsuda, T., Koshiba, S., Tochio, N., Seki, E., Iwasaki, N., Yabuki, T., Inoue, M., Yokoyama, S. & Kigawa, T. (2007). *J. Biomol. NMR*, **37**, 225–229.

Otwinowski, Z. & Minor, W. (1997). *Methods Enzymol.* **276**, 307–326.
Patterson, K. I., Brummer, T., O'Brien, P. M. & Daly, R. J. (2009). *Biochem. J.* **418**, 475–489.
Pawson, T. (1995). *Nature (London)*, **373**, 477–478.
Phan, J., Tropea, J. E. & Waugh, D. S. (2007). *Acta Cryst.* D**63**, 698–704.
Schumacher, M. A., Todd, J. L., Rice, A. E., Tanner, K. G. & Denu, J. M. (2002). *Biochemistry*, **41**, 3009–3017.
Shang, X. *et al.* (2010). *Oncogene*, **29**, 4938–4946.
Takagaki, K., Shima, H., Tanuma, N., Nomura, M., Satoh, T., Watanabe, M. & Kikuchi, K. (2007). *Mol. Cell. Biochem.* **296**, 177–184.
Tanuma, N., Nomura, M., Ikeda, M., Kasugai, I., Tsubaki, Y., Takagaki, K., Kawamura, T., Yamashita, Y., Sato, I., Sato, M., Katakura, R., Kikuchi, K. & Shima, H. (2009). *Oncogene*, **28**, 752–761.
Terwilliger, T. C. & Berendzen, J. (1999). *Acta Cryst.* D**55**, 849–861.
Tonks, N. K. (2006). *Nature Rev. Mol. Cell Biol.* **7**, 833–846.
Vasudevan, S. A., Skoko, J., Wang, K., Burlingame, S. M., Patel, P. N., Lazo, J. S., Nuchtern, J. G. & Yang, J. (2005). *Biochem. Biophys. Res. Commun.* **330**, 511–518.
Vriend, G. (1990). *J. Mol. Graph.* **8**, 52–56.
Wang, J.-Y., Lin, C.-H., Yang, C.-H., Tan, T.-H. & Chen, Y.-R. (2006). *J. Neurochem.* **98**, 89–101.
Wang, J.-Y., Yang, C.-H., Yeh, C.-L., Lin, C.-H. & Chen, Y.-R. (2008). *J. Neurochem.* **107**, 1544–1555.
Wei, C. H., Ryu, S. Y., Jeon, Y. H., Yoon, M. Y., Jeong, D. G., Kim, S. J. & Ryu, S. E. (2011). *Proteins*, **79**, 3242–3246.
Welte, S., Baringhaus, K. H., Schmider, W., Müller, G., Petry, S. & Tennagels, N. (2005). *Anal. Biochem.* **338**, 32–38.
Wiesmann, C., Barr, K. J., Kung, J., Zhu, J., Erlanson, D. A., Shen, W., Fahr, B. J., Zhong, M., Taylor, L., Randal, M., McDowell, R. S. & Hansen, S. K. (2004). *Nature Struct. Mol. Biol.* **11**, 730–737.
Winn, M. D. *et al.* (2011). *Acta Cryst.* D**67**, 235–242.
Yu, W., Imoto, I., Inoue, J., Onda, M., Emi, M. & Inazawa, J. (2007). *Oncogene*, **26**, 1178–1187.
Yuvaniyama, J., Denu, J. M., Dixon, J. E. & Saper, M. A. (1996). *Science*, **272**, 1328–1331.
Zhang, Z.-Y. (2002). *Annu. Rev. Pharmacol. Toxicol.* **42**, 209–234.
Zhang, Z.-Y., Wang, Y. & Dixon, J. E. (1994). *Proc. Natl Acad. Sci. USA*, **91**, 1624–1627.
Zhang, S. & Zhang, Z.-Y. (2007). *Drug Discov. Today*, **12**, 373–381.
Zhou, G., Denu, J. M., Wu, L. & Dixon, J. E. (1994). *J. Biol. Chem.* **269**, 28084–28090.